



Reflectance Mode Fluorescence Optical Tomography with Consumer-Grade Cameras

Mykhaylo Zayats¹(✉), Christopher Hansen², Ronan Cahill³,
Gareth Gallagher³, Ra'ed Malallah^{3,4}, Amit Joshi², and Sergiy Zhuk¹

¹ IBM Research - Europe, Dublin, Ireland

`mykhaylo.zayats1@ibm.com`, `sergiy.zhuk@ie.ibm.com`

² Department of Biomedical Engineering, Medical College of Wisconsin,
Milwaukee, WI, USA

`{chhansen, ajoshi}@mcw.edu`

³ Centre for Precision Surgery, School of Medicine, University College Dublin,
Dublin, Ireland

`{ronan.cahill, gareth.gallagher, raed.malallah}@ucd.ie`

⁴ Physics Department, Faculty of Science, University of Basrah, Garmat Ali, Basra,
Iraq

Abstract. Efficient algorithms for solving inverse optical tomography problems with noisy and sparse measurements are a major challenge for near-infrared fluorescence guided surgery. To address that challenge, we propose an Incremental Fluorescent Target Reconstruction scheme based on the recent advances in convex optimization and sparse regularization. We demonstrate the efficacy of the proposed scheme on continuous wave reflectance mode boundary measurements of emission fluence from a 3D fluorophore target immersed in a tissue like media and acquired by an inexpensive consumer-grade camera.

Keywords: near-infrared imaging · diffuse optical tomography

1 Introduction

Near-infrared (NIR) fluorescence imaging can allow the detection of fluorophores up to 4 cm depth in tissue [11]. Recently, with the availability of clinically approved NIR fluorophores such as indocyanine green or ICG, fluorescence imaging is increasingly being employed for intra-operative guidance during surgically excision of malignant tumors and lymph nodes [6, 15, 16]. Fluorescence imaging is also a workhorse for small animal or preclinical research with multiple commercial devices utilizing sensitive front or back-illuminated and cooled CCD camera detectors available at prices ranging from 250–600K USD [9, 14].

M. Zayats, C. Hansen—These authors contributed equally.

Supplementary Information The online version contains supplementary material available at https://doi.org/10.1007/978-3-031-43999-5_49.

A majority of fluorescence imaging applications including Fluorescence Guided Surgery (FGS) rely upon visible 2D surface imaging [5, 8, 17, 20] while reconstruction of the invisible 3D target in tissue is not widely used for reflectance mode imaging despite a large number of publications in 3D fluorescence diffuse optical tomography (FDOT) since early 1990s [1, 4, 10, 18, 19]. The primary cause of this impasse is the ill-posedness of the mathematical inverse problem underlying the 3D reconstruction of the target in tissue from boundary measurements.

The prime motivation of our work is to enable an efficient 3D tumor shape reconstruction for FGS in an operating room environment, where we do not have full control of the ambient light and we cannot rely on sophisticated time or frequency domain imaging instrumentation and setup. In these situations, one has to use clinical cameras producing rapid Continuous Wave (CW) fluorescence boundary measurements [19] in reflectance mode (i.e., the transmission of the light through the domain is not measured), and with low signal-to-noise ratio which further exacerbates the ill-posedness of FDOT problem. The standard approach for solving FDOT problem with CW measurements is based on Born approximation which works well in the case of a small compared to the computational domain target and a very large number of reflectance-transmission type measurements made by “slow in acquisition” light sources and detector arrays of highly sensitive cooled CCD cameras or photomultiplier tube arrays collecting both reflected and transmitted light [18]. None of these is suitable for FGS settings where time is limited, just a few reflectance mode CW-measurements are available, and the target can be large compared to the imaged domain.

We propose an Incremental Fluorescent Target Reconstruction (IFTR) scheme, based on the recent advances in quadratic and conic convex optimization and sparse regularization, which can recover a relatively large 3D target in tissue-like media. In our experiments, IFTR scheme demonstrates accurate reconstruction of 3D targets from reflectance mode CW-measurements collected at the top surface of the domain. To our best knowledge, this is the first report where the 3D shape of tumor-like target has been recovered from reflectance mode steady-state CW measurements. Previously such results were reported in FDOT literature only for time-consuming frequency-domain or time-domain measurements [12] where photon path-length information is available. Moreover, the data is acquired almost instantly by an inexpensive (<100 Euros) camera with flexible fiber-optics making it suitable for endoscopic FGS in contrast to the standard slow in acquisition frequency-based measurements obtained by expensive (USD100K+ range) stationary cameras. Lastly, IFTR scheme is implemented using FEniCS [3], a high-level Python package for FEM discretization of the physical model, and CVXPY [2, 7], a convex optimization package making this method easy to reuse/adjust for a different setup. The code and data produced for this work are released as an open source at <https://github.com/IBM/DOT>.

2 Methods

Figure 1 describes the setup representing a typical surgical field while excising tumors. We simulate the provision of 3D surgical guidance via a flexible endo-

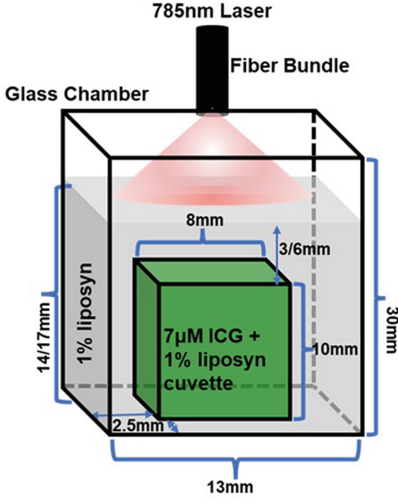


Fig. 1. Schematics of the laboratory experiment setting.

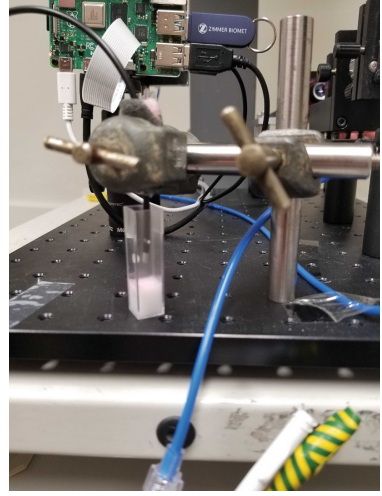


Fig. 2. Depiction of the laboratory experiment setting.

scope type fluorescence imager. For such provision we need to solve the following FDOT problem: estimate the spatial shape χ of the ICG tagged tumor target (the cube in green) within the tissue domain $\Omega \in R^3$ (the area in grey) from measurements y . Measurements are obtained by illuminating the tissue domain with NIR light at ICG peak excitation wavelength via the expanded beam from endoscope fiber bundle, and then measuring the light emitted by the tumor like target diffusing to the top face of the phantom surface $\partial\Omega_{obs}$, by the fiber bundle with suitable emission filter which is coupled to a camera at the backend.

In this section we briefly describe the mathematical formulation of the FDOT problem and introduce the IFTR scheme for solving it.

Forward and Inverse Problems. Photon propagation in tissue-like media is described by a coupled system of elliptic Partial Differential Equations (PDEs) for determining photon fluence ϕ (W/cm^2) at excitation and fluorescence emission wavelengths through out the domain. Wavelength and space dependent absorption and scattering coefficients and fluorophore properties comprise the coefficients of this PDE system (see Appendix A). The discretization of coupled diffusion PDEs is obtained by applying a standard FEM methodology [13]: domain Ω is covered by a uniform grid comprised of N nodes $\{x_i\}_{i=1}^N$; each function ϕ is approximated by a vector $\phi \in \mathbb{R}^N$ with components $\phi_i = \phi(x_i)$; PDEs are approximated using weak formulations incorporating boundary conditions. This results in a system of algebraic equations:

$$\begin{cases} S_x(\chi)\phi_x + M \odot \chi\phi_x = f \\ S_m\phi_m = M \odot \chi\phi_x \end{cases} \quad (1)$$

where the first equation describes the excitation photon fluence $\phi_x \in \mathbb{R}^N$, and the second describes photon emission fluence $\phi_m \in \mathbb{R}^N$; subscripts x and m indicate excitation and emission respectively. Vectors $\mathbf{f}, \boldsymbol{\chi} \in \mathbb{R}^N$ are the source of excitation light and target's shape indicator, i.e., a binary vector such that $\chi_i = 1$ if x_i belongs to the target and 0 otherwise. $S_{x/m}(\cdot) \in \mathbb{R}^{N \times N}$ are the stiffness matrices obtained by discretizing the diffusion terms of excitation/emission PDEs respectively and additionally S_x depends on $\boldsymbol{\chi}$. $M \in \mathbb{R}^{N \times N}$ is the mass matrix and \odot denotes Hadamard (elementwise) product such that $M \odot \boldsymbol{\chi} = M \text{diag}(\boldsymbol{\chi})$ and $M \odot \boldsymbol{\chi} \phi_x = M \odot \phi_x \boldsymbol{\chi}$. Finally, vector of measurements $\mathbf{y} \in \mathbb{R}^K$ is related to the emission fluence ϕ_m as follows

$$\mathbf{y} = T \phi_m \quad (2)$$

Here $T \in \mathbb{R}^{K \times N}$ is a binary matrix that selects components of ϕ_m corresponding to the observed grid nodes and K is a number of observed nodes.

In the following if target indicator $\boldsymbol{\chi}$ is given then the system (1) is referred to as the forward FDOT problem to compute unknown excitation and emission fluence ϕ_x, ϕ_m . If vector $\boldsymbol{\chi}$ is unknown but measurements of emission fluence are present then the system (1)–(2) is referred to as the FDOT inverse problem.

Search Space Regularization. In what follows we propose an algorithm that estimates target's indicator $\boldsymbol{\chi}$ from data \mathbf{y} , i.e. solves the inverse FDOT problem. To reduce the ill-posedness of the inverse problem (1)–(2) we introduce several regularization schemes. These regularizations describe prior knowledge about the desired solution $\boldsymbol{\chi}$ and thus reduce the search space of admissible targets.

The first regularization represents an assumption that the correct $\boldsymbol{\chi}$ is a binary vector. Since binary constraints are not convex, we adopt a more relaxed condition on $\boldsymbol{\chi}$ referred to as the *box constraints*: $0 \leq \chi \leq 1$.

The second regularization describes the piece-wise constant structure of the indicator $\boldsymbol{\chi}$, and is referred to as the *piece-wise total variation* (PTV). It is obtained by extending the notion of total variation which has been successfully applied in optical tomography. To this end, assume $m(j)$, $n(j)$, and $j \in \mathcal{I}$ are indices corresponding to the j -th pair of neighboring nodes. Let the domain Ω be split into N_{ptv} non-overlapping subdomains, e.g., cuboids, and the index \mathcal{I} is correspondingly split into non-overlapping sub-indices \mathcal{I}_i , $i = 1, \dots, N_{ptv}$ of nodes pairs that belong to Ω_i . PTV is obtained as a sum of total variations computed using sub-indices \mathcal{I}_i :

$$v(\boldsymbol{\chi}) = \sum_{i=1}^{N_{ptv}} \sum_{j \in \mathcal{I}_i} |\chi_{m(j)} - \chi_{n(j)}| = \|V\boldsymbol{\chi}\|_1 \quad (3)$$

and is also written in a matrix form assuming matrix V encodes subtraction across node pairs across all sub-indices.

The third regularization aims to reduce a null space of the inverse problem in the boundary layer of a thickness ϵ , reflecting the assumption that the target is

under the surface. It is referred to as the *boundary regularization* and is defined as $W\chi = 0$ where W selects components of χ that belong to the boundary layer.

Finally, the fourth regularization referred to as the *minimum volume regularization* requires that χ has at least m_0 non-zero components: $\mathbb{1}^T \chi \geq m_0$.

Optimization Framework. In this subsection we present an *Incremental Fluorescent Target Reconstruction* (IFTR) scheme solving the inverse problem (1)–(2). Noting that the nonlinearity of the inverse problem stems from the fact that $\chi \odot \phi_x$ is a bi-linear vector function the IFTR scheme employs the following splitting method: (i) for $n = 0, 1, \dots$ fix χ^n and compute ϕ_x^n as the unique solution of linear excitation equation:

$$(S_x(\chi^n) + M \odot \chi^n) \phi_x^n = f \quad (4)$$

then (ii) fix the obtained ϕ_x^n and compute χ^{n+1} as the unique solution of one of the 3 convex optimization problems:

Variant I. This variant relies upon direct inversion of the emission equation matrix S_m^{-1} to find χ^{n+1} :

$$\begin{aligned} \chi^{n+1} = \underset{\chi}{\operatorname{argmin}} \quad & \|\mathbf{y} - TS_m^{-1}M \odot \phi_x^n \chi\|_2^p / \|\mathbf{y}\|_2^p + \|V\chi\|_1 \\ \text{s.t.} \quad & W\chi = 0, \quad \mathbb{1}^T \chi \geq m_0, \quad 0 \leq \chi \leq 1 \end{aligned} \quad (5)$$

Variant II. This variant imposes the emission equation as an inequality constraint:

$$\begin{aligned} \chi^{n+1}, \phi_m^{n+1} = \underset{\chi, \phi_m}{\operatorname{argmin}} \quad & \|\mathbf{y} - T\phi_m\|_2^p / \|\mathbf{y}\|_2^p + \|V\chi\|_1 \\ \text{s.t.} \quad & \langle S_m \phi_m - M \odot \phi_x^n \chi \rangle_p \leq E_m \\ & W\chi = 0, \quad \mathbb{1}^T \chi \geq m_0, \quad 0 \leq \chi \leq 1 \end{aligned} \quad (6)$$

Here, depending on the value of p we take $\langle \mathbf{x} \rangle_1 = \|\mathbf{x}\|_2$ or $\langle \mathbf{x} \rangle_2 = \mathbb{1}^T \mathbf{x}$ and E_m is a parameter defining emission equation constraint tolerance.

Variant III. This variant uses the emission equation as a term of the loss function:

$$\begin{aligned} \chi^{n+1}, \phi_m^{n+1} = \underset{\chi, \phi_m}{\operatorname{argmin}} \quad & \|\mathbf{y} - T\phi_m\|_2^p / \|\mathbf{y}\|_2^p + \|S_m \phi_m - M \odot \phi_x^n \chi\|_2^p + \|V\chi\|_1 \\ \text{s.t.} \quad & W\chi = 0, \quad \mathbb{1}^T \chi \geq m_0, \quad 0 \leq \chi \leq 1 \end{aligned} \quad (7)$$

We note that all the three variants depend on parameter $p = 1, 2$ which defines the type of optimization problem that should be solved: i) if $p = 1$ we get conic optimization problems of the loss function in the form $\|\cdot\|_2$ which would be treated as conic constraints; ii) if $p = 2$ we get quadratic optimization problems.

To get a good initial guess for χ^0 we borrow from the *Born approximation* which suggests that excitation field ϕ_x can be approximated by the background excitation obtained by solving excitation equation with no ICG, i.e., $\chi^0 = 0$.

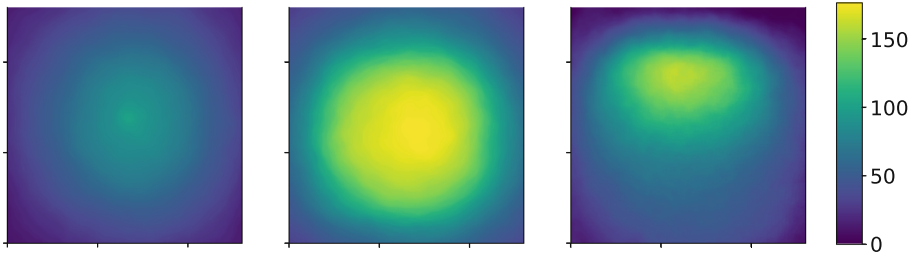


Fig. 3. Emission fluence measured during the laboratory experiment collected on: the top surface from 6 mm deep target (left panel), the top surface from 3 mm deep target (middle panel), the side face $x = 0$ from 3 mm deep target (right panel) and passed through the median filter.

Iterating this splitting method for $n = 0, 1, 2, \dots$ we obtain a sequence of updates χ^n that converge into a vicinity of the true χ provided data is “representative enough”. We conclude the presentation of IFTR scheme with stopping criteria of the iterative process. For this we use a standard Dice coefficient $d(\cdot, \cdot)$ and a binary projector $b(\cdot)$: the scheme stops once the following condition is met

$$d(b(\chi^{n-1}), b(\chi^n)) = 1, \quad [b(\mathbf{x})]_i = \begin{cases} 1, & \text{if } \mathbf{x}_i \geq 0.5 \\ 0, & \text{if } \mathbf{x}_i < 0.5 \end{cases}, \quad d(\mathbf{a}, \mathbf{b}) = \frac{2|\mathbf{a} \cap \mathbf{b}|}{|\mathbf{a}| + |\mathbf{b}|} \quad (8)$$

3 Data Collection

To validate the IFTR scheme, we performed an experiment capturing the essential elements of FGS applications. Figure 1 describes the experiment setup. The tissue phantom was composed of a $13 \times 13 \times 30$ mm (inner dimensions) glass box filled with a 1% liposyn solution, which is a fat emulsion with scattering absorption properties mimicking human soft tissue [12]. The fluorescent target used was a $8 \times 8 \times 8$ mm (inner dimensions) acrylic spectrophotometry cuvette filled with a 5% BSA, 1% liposyn, $7 \mu\text{M}$ ICG solution.

Figure 2 depicts the imaging system consisting of relatively inexpensive components: a Raspberry Pi Computer (4B/2GB), 12MP RGB camera (Raspberry Pi, SC0261) with IR filter removed, 16 mm telephoto lens (Raspberry Pi, SC0123), 700–800 nm band stop filter (Midwest Optical Sytems, DB850-25.4), 785 nm laser (Roithner Lasertechnik, RLTMDL-785-300-5) as the excitation source, and a polyscope fiber bundle (PolyDiagnost, PD-PS-0095). The detector and lens are approximately €100 combined, with just 8 bits of dynamic range. This is in stark contrast to the ultra-sensitive 16-bit scientific cameras priced an order of magnitude more used in other studies.

We collected 3 sets of experimental measurements (see Fig. 3): i) $\mathbf{y}_{top}^{6\text{mm}}$ is emission fluence collected on the top surface from the target immersed 6 mm under the top surface of tissue phantom; ii) $\mathbf{y}_{top}^{3\text{mm}}$ is emission fluence from the target immersed 3 mm under the top surface; and iii) $\mathbf{y}_{top\&side}^{3\text{mm}}$ is also emission

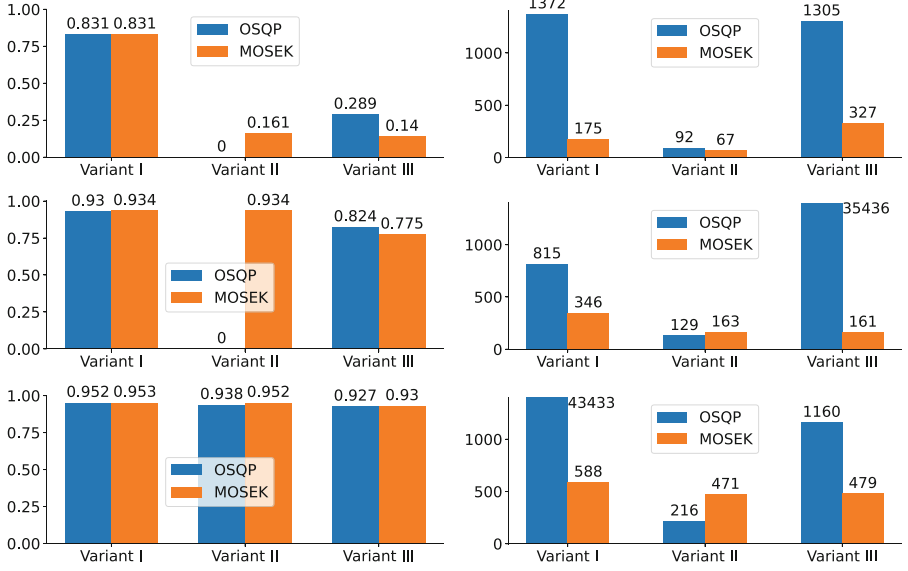


Fig. 4. Dice coefficient (left column) and execution time (right column) of experiments with 3 sets of boundary measurements: 1) y_{top}^{6mm} (top row); 2) y_{top}^{3mm} (middle row) and 3) $y_{top\&side}^{3mm}$ (bottom row).

fluence from the 3 mm deep target which additionally contains measurements taken on a side face ($x = 0$) and then reflected to the other 3 side faces. The raw data was median filtered and re-scaled since the camera we used does not measure fluence in physical units. The re-scaling factor was found by taking the largest value of per pixel division of y_{top}^{3mm} image by the emission fluence computed as a solution of forward FDOT problem with known true target χ_{true} and taken at the top face. It was computed to be 748.4.

4 Experimental Validation

Performance of the proposed IFTR scheme is characterized by a set of numerical experiments. IFTR scheme was implemented using the FEniCS package for FEM matrices computation and CVXPY for the construction of the loss functions and constraints. Additionally CVXPY provides a common interface to various state-of-the-art optimization solvers making it very easy to switch between them. Although we tested IFTR with 4 commonly used solvers: OSQP, SCS and ECOS (distributed together with CVXPY) and MOSEK (required an additional installation) we report results for the solvers that performed the best. Thus, for the quadratic optimization formulation we selected OSQP and for the conic optimization formulation we selected MOSEK. The resulting configurations were compared in terms of Dice coefficient $d(\chi_{est}, \chi_{true})$ comparing estimated target and the true target as well as execution time.

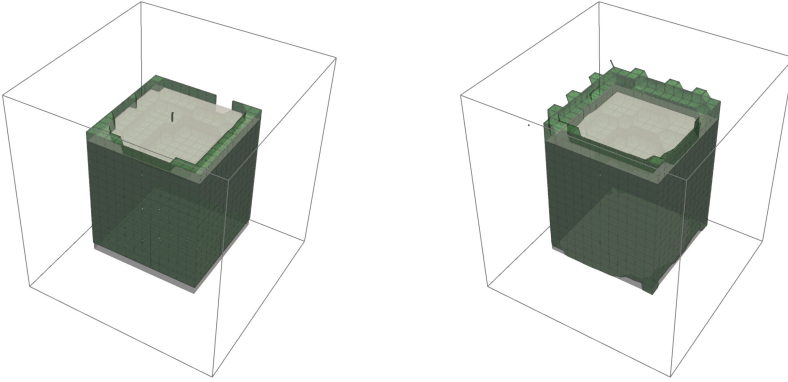


Fig. 5. Reconstructed targets (green) by: IFTR variant I with quadratic OSQP solver from $\mathbf{y}_{top}^{6\text{mm}}$ (left panel); and IFTR variant II with conic MOSEK solver from $\mathbf{y}_{top}^{3\text{mm}}$ (right panel) plotted over the true target (white). (Color figure online)

The results of the performed experiments are summarised in Fig. 4 where the left column of panels presents Dice coefficients and the right column of panels presents respective execution time. Each row of panels in Fig. 4 corresponds (from the top to the bottom) to the experiment using one of three measurements vectors: 1) $\mathbf{y}_{top}^{6\text{mm}}$; 2) $\mathbf{y}_{top}^{3\text{mm}}$ and 3) $\mathbf{y}_{top\&side}^{3\text{mm}}$.

The first experiment is the most challenging as it recovers the target 6 mm deep under the surface. Yet, variant I of IFTR obtains good reconstruction with both quadratic OSQP and conic MOSEK solvers for which Dice score reaches value of 0.831. Good quality reconstruction is indeed confirmed on the left panel in Fig. 5 depicting target recovered by IFTR variant I with quadratic OSQP solver and plotted over the true target. The second experiment recovers the target 3 mm deep which is easier and thus more IFTR variants are capable of obtaining good reconstructions as suggested on the left panel in the middle row in Fig. 4. Additionally, the right panel in Fig. 5 depicts the target reconstructed by IFTR variant II with conic MOSEK solver. We stress that both of these experiments employ reflectance-mode measurements suggesting the proposed IFTR scheme is promising for adoption in FGS-related applications.

The third experiment demonstrates the consistency of IFTR scheme: adding side measurements allows all variants to obtain good reconstructions and further increases Dice coefficients. This, however, comes at a price of increased computational demands, particularly for variant I solved with quadratic OSQP solver. The performed experiments reveal that it is difficult to pick a single winning configuration of IFTR scheme but there are several considerations: i) variant I provides the lowest errors but is the slowest variant with MOSEK solver has been consistently faster than OSQP; ii) variant II is the fastest variant but it is more sensitive to the amount of measurement compared to others; iii) variant III is less sensitive to the amount of measurements compared to Variant II has similar execution time but is less accurate.

We also note that IFTR scheme is robust with respect to PTV regularization parameter. This was achieved by scaling the data misfit and PTV term to similar magnitude: we normalised the misfit term by the norm of the observations vector and rescaled PTV term by the number of subdomains and each local total variation weight by the number of nodes in that subdomain. The robustness to regularization parameter choice was confirmed by our experiments with several different values of such parameter. Another relevant consideration is that PTV impacts the loss function in a different way compared to a standard L1 or L2 regularization: the latter has the unique global minimizer (0-vector) while the former has many global minimizers and IFTR benefits from this.

5 Conclusions

In this work we proposed novel IFTR scheme for solving FDOT problem. It performs a splitting of the bi-linearity of the original non-convex problem into a sequence of convex ones. Additionally, IFTR restricts the search space by a set of regularizers promoting piece-wise constant structure of target's indicator function which in turn allows to recover fluorescent targets from only the reflectance mode CW measurements collected by a consumer grade camera.

Although the scheme was tested using proof-of-concept experimental data and cubical shape target the method is general and depending on mesh discretization level, scalable to arbitrary domain and target shapes. Thus, the obtained results suggest strong potential for adoption of IFTR scheme in FGS related applications.

A Continuous formulation of the FDOT problem

Near-infrared photon propagation in tissue like media is described by the following coupled system of PDEs:

$$-\nabla \cdot (D_x \nabla \phi_x) + k_x \phi_x = 0 \quad (9)$$

$$-\nabla \cdot (D_m \nabla \phi_m) + k_m \phi_m = \Gamma \mu_{axf} \phi_x \quad (10)$$

Here (9) is the excitation equation describing the excitation (at wavelength 785nm) photon fluence $\phi_x, W/cm^2$, and (10) – emission equation describing emission (at wavelength 830 nm) photon fluence $\phi_m, W/cm^2$, subscripts x and m indicate excitation and emission respectively. The parameters of those equations are taken according to the laboratory experiment setup. $\Gamma = 0.016$ is a constant representing the dimensionless quantum efficiency of ICG fluorescence emission. $D_{x/m}, cm$ and $k_{x/m}, cm^{-1}$ refer to coefficients in excitation and emission equations, which determine light scattering and absorption properties of tissues:

$$D_{x/m} = \frac{1}{3 \left(\mu_{ax/mi} + \mu_{ax/mf} + \mu'_{sx/m} \right)}, \quad k_{x/m} = \mu_{ax/mi} + \mu_{ax/mf} \quad (11)$$

where $\mu'_{sx} = 9.84 \text{ cm}^{-1}$ and $\mu'_{sm} = 9.84 \text{ cm}^{-1}$ are the scattering coefficients of Liposyn at excitation and emission wavelength respectively; $\mu_{axi} = 0.023 \text{ cm}^{-1}$ and $\mu_{ami} = 0.0289 \text{ cm}^{-1}$ are the absorption coefficients of Liposyn at excitation and emission wavelengths; $\mu_{axf} = \mu_{ICG}\chi$, cm^{-1} is the absorption coefficient of the unknown ICG-tagged target and thus depends on the target's shape modelled by an indicator function χ and ICG absorption coefficient at excitation wavelength $\mu_{ICG} = 3.5 \text{ cm}^{-1}$; $\mu_{amf} = 0 \text{ cm}^{-1}$ as we assume there is no self-absorption of ICG fluorescence emission at the concentration ranges employed in this work and for practical applications [12].

The system (9)–(10) is complemented by Robin-type boundary conditions modelling the excitation source applied at the surface of the domain Ω :

$$\gamma\phi_x + 2D_x \frac{\partial\phi_x}{\partial\mathbf{n}} + S = 0 \quad (12)$$

$$\gamma\phi_m + 2D_m \frac{\partial\phi_m}{\partial\mathbf{n}} = 0 \quad (13)$$

where $\gamma = 2.5156$ – dimensionless constant depending on the optical reflective index mismatch at the boundary.

References

1. Abascal, J.J., et al.: Fluorescence diffuse optical tomography using the split Bregman method. *Med. Phys.* **38**(11), 6275–6284 (2011)
2. Agrawal, A., Verschueren, R., Diamond, S., Boyd, S.: A rewriting system for convex optimization problems. *J. Control Decis.* **5**(1), 42–60 (2018)
3. Alnaes, M.S., et al.: The FEniCS project version 1.5. *Arch. Numer. Softw.* **3**, 1–15 (2015)
4. Arridge, S.R., Schotland, J.C.: Optical tomography: forward and inverse problems. *Inverse Prob.* **25**(12), 123010 (2009)
5. Cahill, R.A., et al.: Artificial intelligence indocyanine green (ICG) perfusion for colorectal cancer intra-operative tissue classification. *Br. J. Surg.* **108**(1), 5–9 (2021)
6. Cho, S.S., Salinas, R., Lee, J.Y.: Indocyanine-green for fluorescence-guided surgery of brain tumors: evidence, techniques, and practical experience. *Front. Surg.* **6**, 11 (2019)
7. Diamond, S., Boyd, S.: CVXPY: a python-embedded modeling language for convex optimization. *J. Mach. Learn. Res.* **17**(83), 1–5 (2016)
8. Epperlein, J., et al.: Practical perfusion quantification in multispectral endoscopic video: Using the minutes after ICG administration to assess tissue pathology. In: *AMIA Annual Symposium Proceedings* (2021)
9. Graves, E., Weissleder, R., Ntziachristos, V.: Fluorescence molecular imaging of small animal tumor models. *Curr. Mol. Med.* **4**(4), 419–430 (2004)
10. Hoshi, Y., Yamada, Y.: Overview of diffuse optical tomography and its clinical applications. *J. Biomed. Opt.* **21**(9), 091312–091312 (2016)
11. Houston, J.P., Thompson, A.B., Gurfinkel, M., Sevic-Muraca, E.M.: Sensitivity and depth penetration of continuous wave versus frequency-domain photon migration near-infrared fluorescence contrast-enhanced imaging. *Photochem. Photobiol.* **77**(4), 420–430 (2003)

12. Joshi, A., Bangerth, W., Hwang, K., Rasmussen, J.C., Sevik-Muraca, E.M.: Fully adaptive fem based fluorescence optical tomography from time-dependent measurements with area illumination and detection. *Med. Phys.* **33**(5), 1299–1310 (2006). <https://doi.org/10.1118/1.2190330>, <https://aapm.onlinelibrary.wiley.com/doi/abs/10.1118/1.2190330>
13. Langtangen, H.P., Logg, A.: *Solving PDEs in Python*. Springer, Cham (2016). <https://doi.org/10.1007/978-3-319-52462-7>
14. Leblond, F., Davis, S.C., Valdés, P.A., Pogue, B.W.: Pre-clinical whole-body fluorescence imaging: review of instruments, methods and applications. *J. Photochem. Photobiol. B* **98**(1), 77–94 (2010)
15. Low, P.S., Singhal, S., Srinivasarao, M.: Fluorescence-guided surgery of cancer: applications, tools and perspectives. *Curr. Opin. Chem. Biol.* **45**, 64–72 (2018)
16. Nagaya, T., Nakamura, Y.A., Choyke, P.L., Kobayashi, H.: Fluorescence-guided surgery. *Front. Oncol.* **7**, 314 (2017)
17. Shafiee, S., et al.: Dynamic NIR fluorescence imaging and machine learning framework for stratifying high vs low notch-dll4 expressing host microenvironment in triple-negative breast cancer. *Cancers* **15**(5), 1460 (2023)
18. Stuker, F., Ripoll, J., Rudin, M.: Fluorescence molecular tomography: principles and potential for pharmaceutical research. *Pharmaceutics* **3**(2), 229–274 (2011)
19. Yamada, Y., Okawa, S.: Diffuse optical tomography: present status and its future. *Opt. Rev.* **21**(3), 185–205 (2014)
20. Zhuk, S., et al.: Perfusion quantification from endoscopic videos: learning to read tumor signatures. In: Martel, A.L., et al. (eds.) *MICCAI 2020*. LNCS, vol. 12263, pp. 711–721. Springer, Cham (2020). https://doi.org/10.1007/978-3-030-59716-0_68